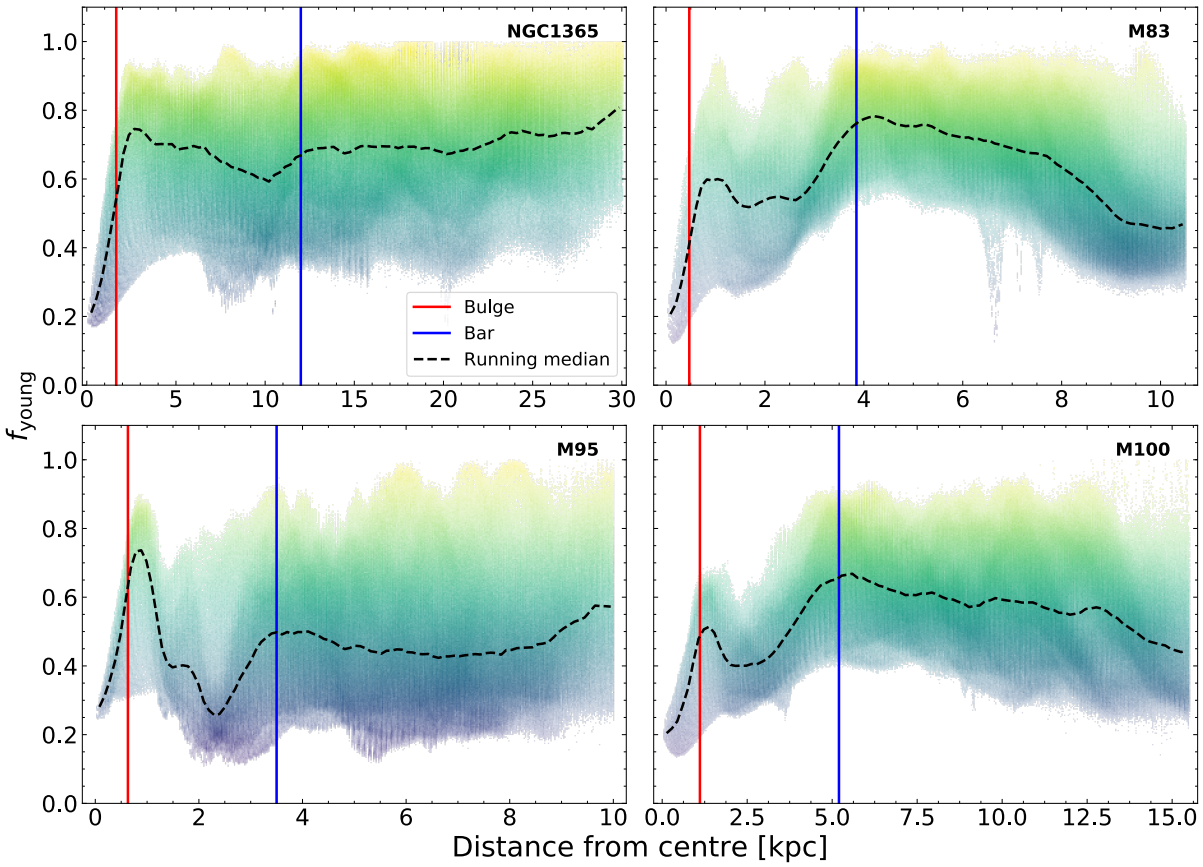

Fig. 7. Distribution of f_{young} calculated for every galaxy with galactocentric distance. Each point represents a dust cell and it is colour-coded according to f_{young}. The level of transparency indicates the points density. The radius of the bulge is indicated with a vertical red line while the vertical blue line denotes the outer truncation radius of the Ferrers-bar. The dashed black line is the running median through the data points.

using the prescription provided in Kennicutt & Evans (2012). To calculate the sSFR in every data cell, we simply divided the SFR with the stellar mass. To fit the relationship of Fig. 8, we used the function given in Leja et al. (2019) (see their Eq. (2)) which yields the following relation:

$$f_{\rm young} = \frac{1}{2}\left[1 - \tanh\left(a \log\left({\rm sSFR/yr^{-1}}\right) + bz + c\right)\right]. \quad (4)$$

where $a = -0.87$ and $c = -9.3$. Since the galaxies in our sample lie in the local Universe ($z < 0.01$) we used $z = 0$. For comparison purposes, we provide the best-fitted power-laws of: M 31 (Viaene et al. 2017), M 51 (De Looze et al. 2014), and the relations derived by Leja et al. (2019) for a sample of galaxies from the 3D-HST catalogues at redshift $0.5 < z < 2.5$. Due to the overlap of colours, we present the data of the radiation transfer models of each galaxy separately in Fig. C.1, and fit the data cells using both Eq. (4) and a power-law. The best-fitted parameters are given in Table C.1.

It is immediately evident that there is an increasing trend between the young heating fraction in each dust cell and the sSFR in all cases. Cells of high sSFR ($>10^{-10}$ yr^{-1}) are primarily heated by the young stellar populations, whereas the contribution of the old population becomes more and more significant for cells with low sSFR ($\leq 10^{-10}$ yr^{-1}). The bulk of data points of every galaxy are concentrated more or less in the same region of the diagram, with the sSFR spanning three orders of magnitude. Our results are in accordance with the relations produced by the radiation transfer models of M 31 and M 51 despite the overall differences and assumptions made in the studies of Viaene et al. (2017) and De Looze et al. (2014), respectively (i.e. different ages of the young stellar populations and different methods of estimating the sSFR). The derived relationship, in principle, will enable us to quantify the young heating fraction based on sSFR measurements in other galaxies and can be applied to calibrate the energy fraction of the old stellar population in global SED modelling.

Furthermore, we find very good agreement with the relations derived by Leja et al. (2019) at different redshifts. The authors fitted the data of more than ~50 000 galaxies from the 3D-HST catalogues at redshifts $0.5 < z < 2.5$. Galaxies at those redshifts are massive and obscured star formation is the main agent of star formation (Whitaker et al. 2017). The authors used the Prospector-α physical model (Leja et al. 2017) to fit the galaxy SEDs. The model includes a flexible non-parametric star-formation history (SFH), a two-component dust attenuation model with a flexible age-dependent Charlot & Fall (2000) attenuation curve, a model accounting for the MIR emission from AGN torii, and dust emission via energy balance. In their study, the young heating fraction is defined as the relevant fraction of $L_{\rm UV+IR}$ emitted by the young stars ($\leq$100 Myr), while a Chabrier (2003) IMF was used. After fitting the data, the authors reported lower SFRs and higher stellar masses than those found by previous studies in the literature for galaxies at $0.5 < z < 2.5$. They infer that the cause for this offset in both quantities is the contribution from the old stars (>100 Myr), implying an older, less active Universe. Here we notice that the relation yielded by Eq. (4) shifts towards higher sSFR values with increasing redshift (from the solid black line to the dashed blue line). It is

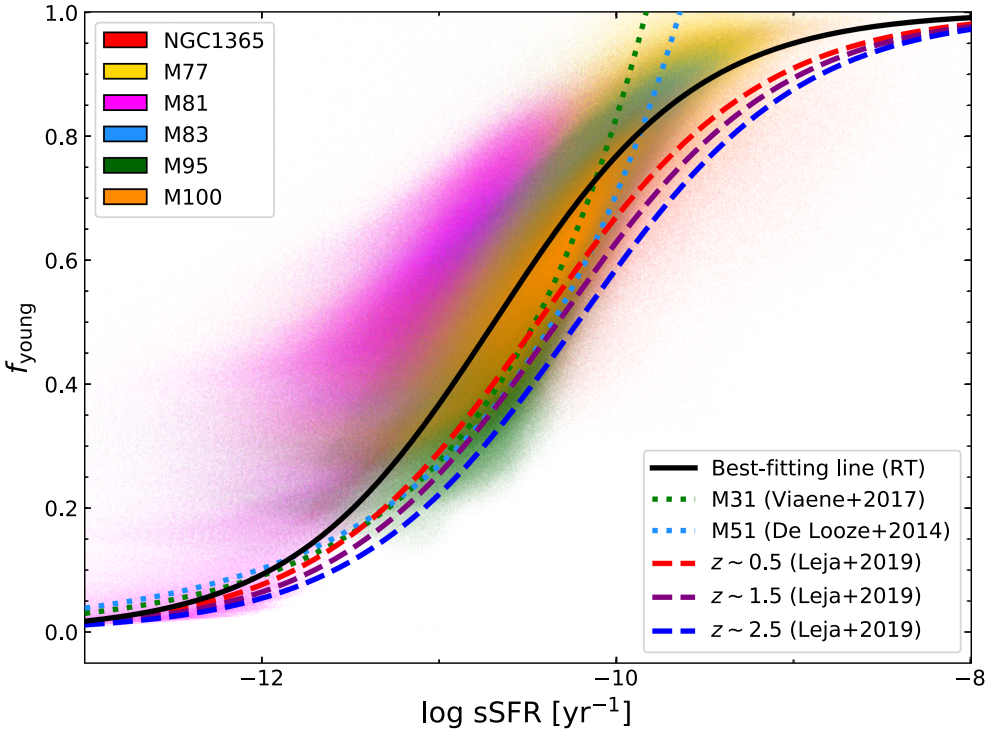

Fig. 8. Relation between sSFR and $f_{\rm young}$, shown for the radiation transfer models of: NGC 1365, M 83, M 95, M 100 (this work); M 81 (Verstocken et al. 2020); and M 77 (Viaene et al. 2020). Each galaxy dataset is assigned with a different colour indicated in the upper left corner of the figure. The solid black line shows the fit from Eq. (4) through all data cells of every galaxy (RT). For comparison purposes we also provide the best-fitted power-laws of: M 31 (dotted green line, Viaene et al. 2017); M 51 (dotted cyan line, De Looze et al. 2014); and the relations derived by Leja et al. (2019) for a sample of galaxies from the 3D-HST catalogues at three redshift bins: $z \sim 0.5$ (dashed red line), $z \sim 1.5$ (dashed purple line), and $z \sim 2.5$ (dashed blue line).

also worth noting that for a fixed sSFR value the $f_{\rm young}$ decreases with increasing redshift. To some degree the shift of the sSFR–$f_{\rm young}$ relation towards higher sSFR values with increasing redshift can be attributed to the increased SFR, at least in the regime $0.5 < z < 1.5$. In addition, Leja et al. (2019) showed that the old stellar populations in high-redshifts ($1.5 < z < 2.5$) are relatively younger and on average more luminous, contributing more to the dust heating, which explains the decrease in $f_{\rm young}$ with redshift.

The concluding remarks in Leja et al. (2019) agree quite well with the picture we draw here by studying the properties of local galaxies on resolved scales, as we also infer that the older stellar population has a more prominent role on the heating of the diffuse dust. The relation between the sSFR and the relative fraction of dust heated by the star-forming regions or by the old stellar populations has now been observed in a wide range of galaxy types and using various modelling approaches. Our analysis showcases the importance of a consistent modelling approach in order to derive safe conclusions when comparing different datasets. With that in mind, further investigation of the relationship discussed here, both in global and resolved scales, will allow for a better understanding of the scatter in the sSFR–$f_{\rm young}$ relation.

5.4. Dust temperature

Light originating from star-forming regions acts as an important dust-heating source and thus one should expect to find a trend between regions of high dust temperatures and increased levels of star formation. Moreover, several studies have shown a dependence of the FIR surface brightness colours (i.e. indicators of dust temperature), with radius (Bendo et al. 2010, 2012). In the left column of Fig. 9 we plot the dust temperature ($T_{\rm dust}$) as a function of the deprojected galactocentric radius in kpc. Again, each point on each panel of this plot represents a dust cell in our simulations, colour-coded according to $f_{\rm young}$. The bulge radius is indicated with a vertical red line while the outer truncation radius of the Ferrers-bar profile is indicated with the vertical blue line. From our analysis it is possible to determine how much the old stellar bulge and the composite stellar populations of the bar and disc structures affect the temperature of the diffuse dust.

Here we should make clear to the reader that the dust temperatures are only those of the diffuse dust and thus interpretation of the results should be considered with caution. Including the dense dust clouds in the star-forming regions, which they are subgrid properties of the MAPPINGS III templates, could add a significant amount of unusually high SFR and temperature values.

The diffuse dust temperature of each dust cell in our simulations was approximated through the strength of the ISRF (U). First we calculated U by integrating the mean intensity of the radiation field J_λ of each cell over the wavelength range 8–1000 μm. Then we normalised with the ISRF, estimated by Mathis et al. (1983) for the solar neighbourhood ($\sim 5\times10^{-6}$ W m^{-2}). Assuming that dust is heated by an ISRF with a Milky-Way like spectrum (Mathis et al. 1983) we employed the following equation to approximate the dust temperatures of the diffuse dust:

$$T_{\rm dust} = T_{\rm o}\, U^{1/(4+\beta)}, \tag{5}$$

(Nersesian et al. 2019, and references therein). Here, $T_{\rm o} = 18.3$ K which is the dust temperature measured in the solar neighbourhood, and β is the dust emissivity index, which, for the THEMIS dust model, gives the value of 1.79.

Overall, temperatures range from 13–37 K with a decreasing trend towards the outermost regions of each galaxy, with several peaks and fluctuations which coincide with the appearance of high young heating fractions. These peaks are star-forming regions in the spiral arms or in the galactic disc, with the harsh UV radiation by the young populations heating the dust grains to high temperatures (25–37 K). Again, if we follow the running median line, a distinct pattern is seen in all galaxies. Dust temperature peaks at the centre of each galaxy and then sharply declines until a plateau is reached, approximately at 20–25 K (even with a rising trend, more clearly visible in the cases of